Chapter-6 Structural and Electrical Properties of Dy-doped..

6.1 Introduction

Over the past few years, several materials have been investigated as anode materials for SOFC application [167]. Generally, Ni-YSZ based anode is used for SOFC, although facing long-term instability issues and suffering from carbon and sulfur poisoning and agglomeration of nickel particles at elevated temperature [168], [169]. Therefore, development of new alternative anode materials able to withstand redox cycling and hydrocarbon fuels is needed. Doped $SrTiO_3$ materials are promising candidates for anode of SOFCs as discussed in previous chapters. $SrTiO_3$ based perovskite materials are potential mixed ionic-electronic conductors to anodic reaction which may resolve the issue of carbon and sulfur poisoning at reaction sites along with excellent thermal and chemical stability [59], [170]–[172]. However, pure $SrTiO_3$ cannot be used as anode materials due to its low electrical conductivity. Therefore, donor doped $SrTiO_3$ have been developed to enhance the electrical conductivity under reducing conditions [66]. Under reducing atmosphere, redox coupling (Ti^{4+}/Ti^{3+}) occurs in $SrTiO_3$ which exhibits an n-type semiconducting behavior. Several rare earths were tested as possible donor materials, La [70], [173], Nb [174], Y [38], [173], [175], Sm [156]. Some papers report investigations on Dy-doped $SrTiO_3$ for application in energy storage systems [176], [177]. However, this system has not been tested as SOFC material until now.

The ionic radius of Dy^{3+} (1.23 Å, CN 12) is close to that of Sr^{2+} (1.44 Å, CN 12) [178], indicating that incorporation of Dy^{3+} is sterically favored at Sr-site. Lattice defect structure must be modified to maintain electro-neutrality due to charge imbalance between Dy^{3+} and Sr^{2+} ions, for instance with formation of oxygen-rich planes improving the ionic conductivity of Dy-doped $SrTiO_3$ [66], [104], [107]. In addition, Liu a et al.

[179] reported high electronic conductivity of reduced Dy-doped $SrTiO_3$, indicating that it can be considered as anodic materials for SOFC.

In present chapter, the influence of Dy content on the structural and electrical behavior of $SrTiO_3$ prepared by auto-combustion route was studied. Properties were measured both in air and hydrogen atmosphere and discussed in detail.

6.2 Results and Discussion

6.2.1 Structural Studies

X-ray diffraction patterns samples DST3-DST10, sintered in air, are shown in fig. 6.1, within the results of Rietveld refinement. All samples show cubic phase with space group $Pm\bar{3}m$ (JCPDS Card Number: 86-0178). No impurity peaks were detected for the samples with $x \leq 0.05$, while traces of secondary phases were observed in the samples with $x \geq 0.08$. In particular, TiO_2 (JCPDS Card Number: 21-1276) and Dy_2O_3 (JCPDS Card Number: 01-078-0388) in DST8 and, TiO_2 and $Dy_2Ti_2O_7$ (JCPDS Card Number: 17-0453) were observed in DST10, respectively. The lattice parameters and some reliability factors of RR are summarized in table 6.1. From this table, it is observed that, lattice parameter decreases with increase in Dy content, which may be attributed to the replacement of the larger sized Sr^{2+} ions at A-sites of the perovskite structure by the smaller Dy^{3+} ions. Moreover, in all the refinements, the reliability factors are satisfactory, indicating a good refined crystal structure model representative of the real case. In case of DST8 and DST10, RR was performed considering also the secondary phases, whose amount were evaluated as 3.5 wt.% of TiO_2 and 3 wt.% of Dy_2O_3 in DST8, and 3 wt.% of TiO_2 and 2.4 wt.% $Dy_2Ti_2O_7$ in DST10.

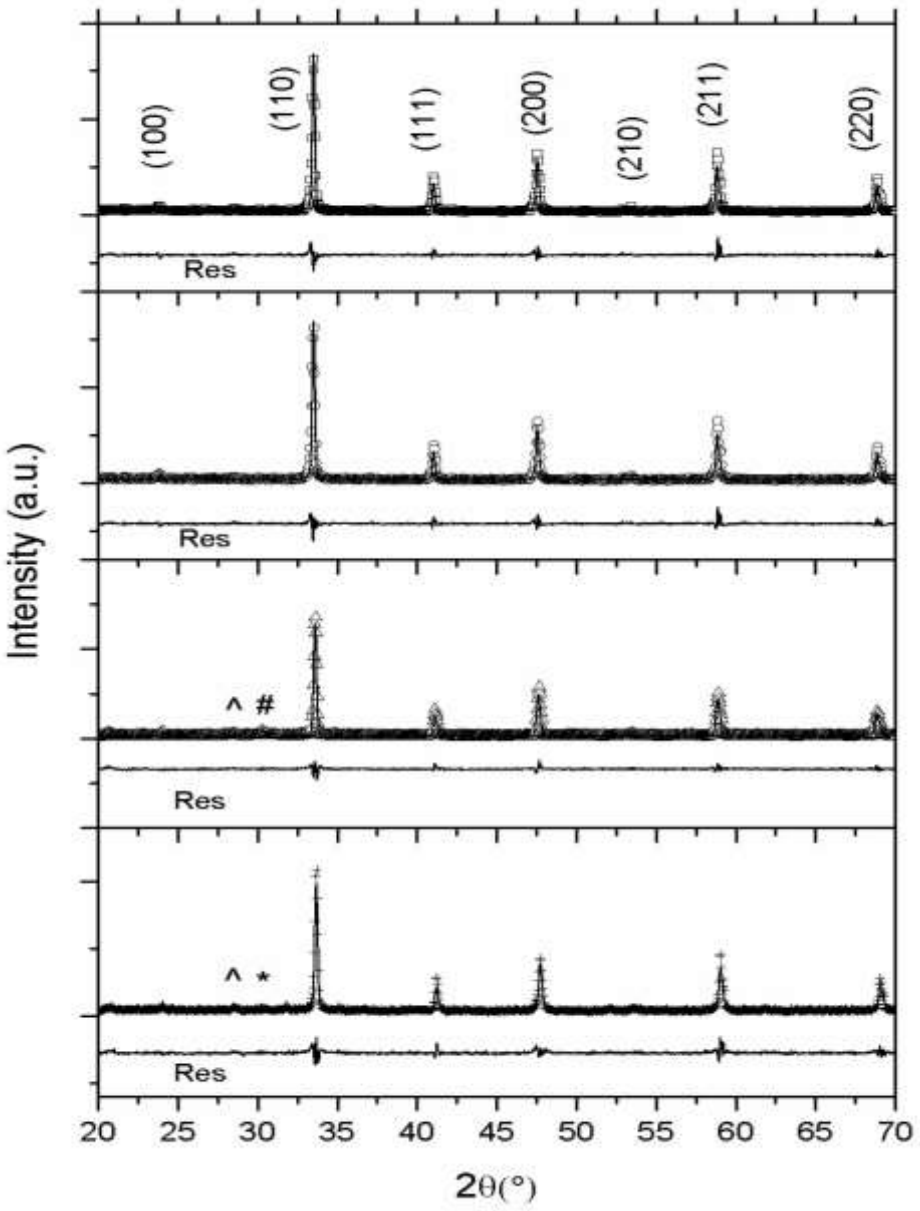

Figure 6.1: Rietveld refinement (-) of XRD patterns (□ = DST3, ○ = DST5, Δ = DST8 and + = DST10). Residuals (Res) and Miller indexes are also reported with major reflections of TiO_2 (^), Dy_2O_3 (#) and $Dy_2Ti_2O_7$ (*) secondary phases.

In fig. 6.2, the microstrain and crystallite size of the studied compositions are reported by Williamson-Hall model using eq. (2.1). Both variables show the same trend, being, the minimum value of microstrain and crystallite size, observed for the sample DST8.

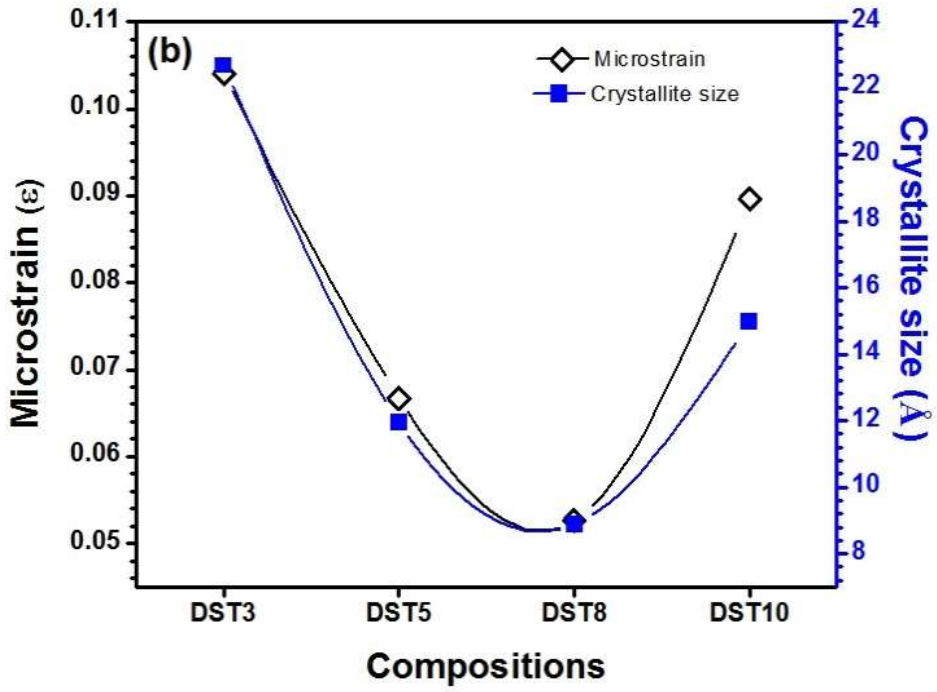

Figure 6.2: The calculated microstrain and crystallite size as function of Dy amount.

6.2.2 Microstructural Analysis

DST8 showed also the minimum of relative density, as reported in table 6.1, that was confirmed by comparison of FESEM micrographs of fractured samples sintered at 1200 ºC in air (fig. 6.3). The average grain size was also determined using ImageJ software, and was found to be 4.54 µm, 1.62 µm, 1.06 µm and 5.13 µm for DST3, DST5, DST8 and DST10, respectively. This trend can be considered as an effect of dopant segregation at the grain boundary, which inhibits the grain growth during sintering. In fact, segregation is known to be driven by the decrease in interfacial free energy that accompanies the densification process and is therefore a general feature of polycrystalline ceramics [153]. When dopant segregates in a secondary phase, that is the case of DST10, this effect is not more present; on the contrary this secondary phase can promote the increasing of grain size and densification [180].

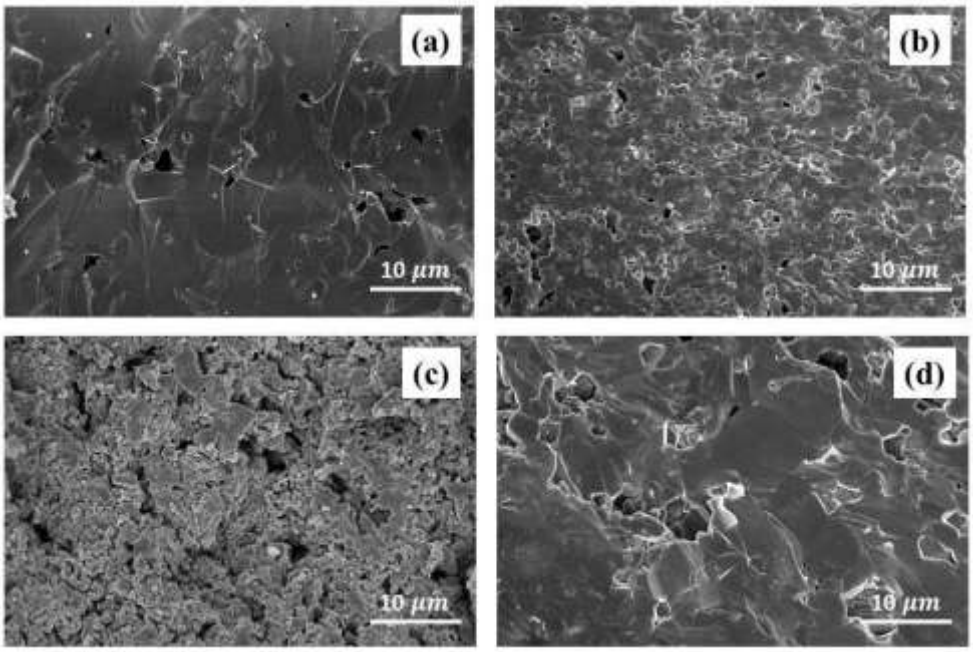

Figure 6.3: The FESEM micrographs of fractured compositions (a) DST3, (b) DST5, (c) DST8 and (d) DST10.

Table 6.1: Rietveld refined parameters and relative density of studied compositions.

Sample	Lattice Parameter (Å)	$\chi 2$	R_B	R_F	Relative density (%)
DST3	3.91078	6.464	5.31	3.71	97.7
DST5	3.90996	6.19	4.75	3.75	95.7
DST8	3.90906	5.75	4.83	3.74	66.4
DST10	3.90823	6.68	5.29	4.03	87.9

6.2.3 Impedance Analysis and Chemical Stability

Impedance measurements of all compositions were collected in air and hydrogen, at different temperatures. As an example, impedance spectra of DST3 sample, measured in air at different temperatures are reported in fig. 6.4. As expected, for all compositions, spectra shift towards higher frequency when temperature is increased, mainly due to a decrease of resistance.

Spectra obtained at various temperatures on samples with different Dy content are reported in fig. 6.5, where data are represented as Nyquist plots of imaginary (Z″) vs. real

(Z′) impedance. One depressed semi-circle was observed in all cases, that was fitted by an equivalent circuit consisting by one parallel R-CPE element (R//Q) in series to a resistance R_0 simulating the contact resistance. The fitted R values were utilized to calculate the conductivity σ_p by following the equation:

$$\sigma_p = l/RS \tag{6.1}$$

where l is the thickness and S is the cross sectional surface area of specimens.

After reduction, electronic conductivity measured in hydrogen increased significantly; under this circumstance, reactance was negligible and R, for each composition and temperature, was obtained from the real part of impedance only.

Conductivity was also corrected for porosity by following the Bruggeman Asymmetric Model [181], [182]. The model treats a continuous phase of conductivity σ_1 with an embedded discontinuous phase σ_2 and a volume fraction x_2:

$$(\sigma_1/\sigma_m) \cdot (\sigma_m - \sigma_2/\sigma_1 - \sigma_2)^3 = (1 - x_2)^3 \tag{6.2}$$

where σ_m is the conductivity of dispersion. In this case, x_2 is the porosity x_p, (as calculated from density reported in table 6.1) and then σ_2 = 0 as the phase 2 corresponds to pores; $\sigma_1 = \sigma$ is the true conductivity of dense Dy-doped $SrTiO_3$, and σ_m is σ_p, the measured effective conductivity of porous pellet. In this hypothesis, eq. (6.2) can be written as:

$$\sigma = \sigma_p/\left(1 - x_p\right)^{3/2} \tag{6.3}$$

In table 6.2, corrected conductivity values, σ, obtained in air and in hydrogen at 650 °C, a standard operative temperature for a SOFC, are reported as function of Dy content. Moreover, Arrhenius plots of conductivity in air and hydrogen, obtained for all compositions, are presented in fig. 6.6 and the activation energy (E_a), for conduction

mechanism in air and hydrogen, was also reported in table 6.2 as calculated from fitting of conductivity data to the Arrhenius relation.

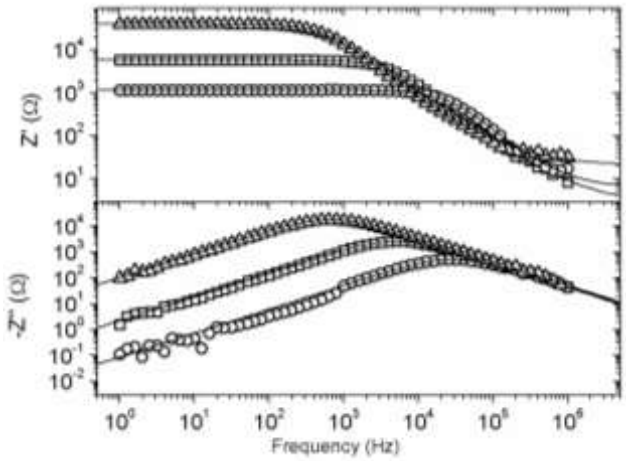

Figure 6.4: Impedance spectra of DST3 sample, measured in air, at: (Δ) 232 °C, (□) 305 °C, (○) 380 °C.

Table 6.2: Conductivity values (σ) measured at 650 °C and calculated energy activations (E_a) of conduction mechanism, for all composition, respectively in air and in hydrogen.

Sample	**σ (650 °C, O_2) $\times 10^{-2}$ Scm^{-1}**	**σ (650 °C, H_2) $\times 10^{-2}$ Scm^{-1}**	**E_a (O_2) eV**	**E_a (H_2) eV**
DST3	7.16×10^{-1}	3.125	0.77	0.17
DST5	9.88×10^{-1}	3.054	0.66	0.21
DST8	2×10^{-3}	13.639	1.42	0.10
DST10	4.4×10^{-2}	1.221	1.26	0.24

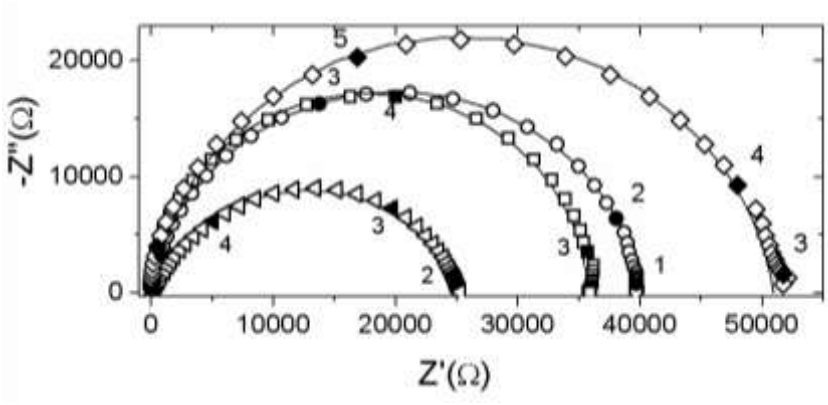

Figure 6.5: Nyquist plot of impedances measured in air, at several temperatures, as reported by symbols: (Δ) DST10 at 459 °C, (□) DST5 at 174 °C, (○) DST3 at 232 °C, (◇) DST8 at 515 °C. The solid line was obtained by fitting the data with the equivalent circuit, as reported in the text. Dark markers point at measurement frequency.

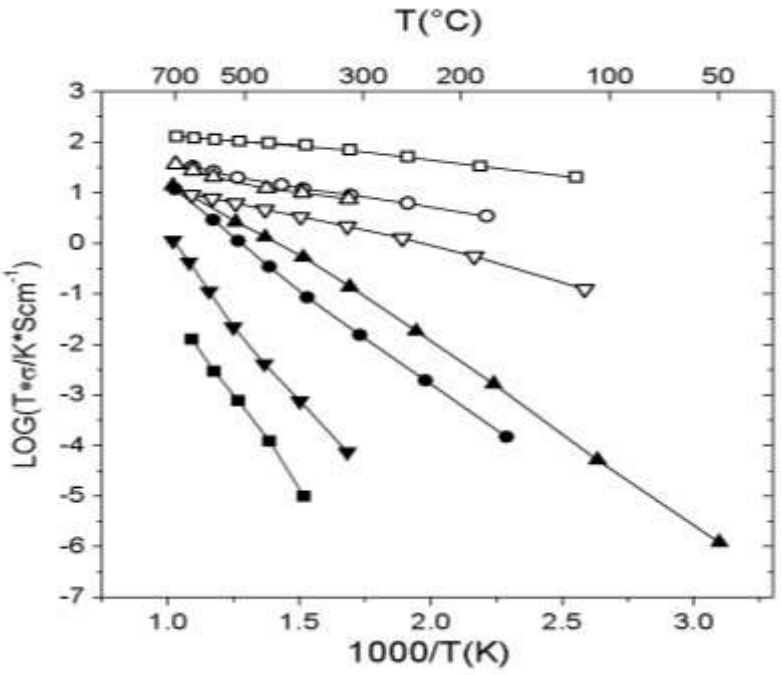

Figure 6.6: Arrhenius plot of conductivity of DST3 (●), DST5 (▲), DST8 (■) and DST10 (▼), samples as function of temperature, in air (full symbols) and in hydrogen (empty symbols). Lines are the best fit of Arrhenius relation to experimental data.

It is observed that conductivity, for all composition, increases passing from air to hydrogen. DST5 showed the highest conductivity in air whereas DST8 in H_2 atmosphere. The activation energy calculated for all compositions is listed in table 6.2. It can be noted that in air E_a values are generally lower for samples DST3 and DST5, suggesting electronic nature of conductivity. On the contrary, for DST8 and DST10, conductivity is more ionic. After reduction with H_2 the activation energy is further lowered, being in the range of 0.1 - 0.24 eV for all samples. Above reported experimental observations can be explained by considering the incorporation mechanisms of dopant into the perovskite structure of $SrTiO_3$. Given the average value of ionic radius of Dy^{3+} in 6-fold coordination (0.91 Å) and in 12-fold coordination (1.23 Å) [173], three types of incorporation can be considered and expressed by the following equations written with the Kröger-Vink notation:

$$Dy_2O_3 + 2TiO_2 \xrightarrow{SrTiO_3} 2Dy_{Sr}^{\cdot} + 2Ti_{Ti}' + 6O_O^X + 1/2\,O_2 \qquad (6.4)$$

$$Dy_2O_3 \xrightarrow{SrTiO_3} Dy_{Sr}^{\cdot} + Dy_{Ti}' + 3O_O^X \quad (6.5)$$

$$Dy_2O_3 \xrightarrow{SrTiO_3} 2Dy_{Ti}' + V_O^{\cdot\cdot} + 3O_O^X \quad (6.6)$$

Equation (6.4), accounts for the incorporation at the Sr-site, with formation of positively charged defects, compensated by electrons or, equivalently, by partial reduction of Ti^{4+} to Ti^{3+}. In the second case, eq. (6.5), the incorporation takes place both at Sr- and Ti-sites, with self-compensation of charges. Finally, eq. (6.6) is relevant to the case of incorporation at the Ti-site with formation of negatively charged defects, compensated by oxygen vacancies.

As already reported in case of $BaTiO_3$ [78], the most energetically favorable incorporation mechanism for Dy^{3+} and similar rare-earths like Y, Er and Gd, is the self-compensation. However, other factors can determine the actual incorporation mechanism, the most important being the amount of dopant, the cationic ratio and the temperature.

Lattice parameters and strain are determined by the incorporation mechanism so that, minimal local distortion (microstrain) can be expected when Dy^{3+} is replacing both (larger) Sr^{2+} and (smaller, being its ionic radius in 6-fold coordination equal to 0.61 Å) Ti^{4+} atoms. The formation of the pyroclore phase also introduces point defects, namely Ti vacancies, which affect the lattice size and strain state.

Moreover, results indicate that there is a regime change for $x \geq 0.08$, passing from a conductivity substantially electronic type ($x \leq 0.05$) to a one ionic type ($x \geq 0.08$) with a significant decreasing of conductivity value (≈ 2 orders of magnitude at 650 °C). In both the two regimes, increasing Dy content the conductivity increases.

Therefore, for DST8 self-compensation (eq. (6.5)) is mainly active, which also reflect in lower conductivity and high Ea, and causing the smaller microstrain and negligible amount of electrons, being the conduction of ionic nature and due to oxygen

vacancies produced either intrinsically (Schottky disorder) or partially through mechanism of eq. (6.6). Mechanism of eq. (6.6) is mainly active in samples DST10, as demonstrated by higher conductivity, lower Ea and higher microstrain. In these samples, however, the presence of a secondary phase, i.e. of Ti vacances in the main phase, may account for observed lowering of the unit cell volume.

Conversely, in case of DST3 and DST5, both the eq. (6.4) and (6.5) take place, giving higher microstrain, higher conductivity and lower Ea (ionic-electronic). The lattice oxygen may be lost and thus oxygen vacancies will be generated under reducing atmosphere as per eq. (1.19) and to preserve the electro-neutrality, the following equation must be satisfied.

$$[Ti'_{Ti}] = [Dy^{\bullet}_{Sr}] + 2[V_O^{\bullet\bullet}] \qquad (6.7)$$

Therefore, both extrinsic defects introduced by Dy incorporation at Sr-site and intrinsic oxygen vacancies, which are formed under reducing conditions, contribute to the formation of electrons and increase of conductivity.

The conductivity of all samples is actually increased after exposure to hydrogen atmosphere; the higher value for conductivity was found for sample DST8, decreasing to about half in DST3 and DST5 and by one order of magnitude in DST10 at 650 ºC. By XRD measurement, repeated after the reduction it is observed that DST10 degraded after reduction. Results are reported in fig. 6.7, together with the patterns obtained after sintering in air and discussed above. It is clear that XRD patterns of DST3 and DST5 overlap with each other, showing only the presence of a small quantity of TiO_2.

On the contrary, in the other two samples DST8 and DST10 after reduction additional phases were also found, that are Ti-Sr mixed oxides with different stoichiometry. This Phenomenon is less prominent in DST8 and it doesn’t affect the

conductivity, while DST10 was strongly degraded and its conductivity decreased strongly.

In light of these results, the most promising candidate for use as anodic material in SOFC is composition $Dy_{0.08}Sr_{0.92}TiO_3$ due to its sufficient chemical stability both under reducing and oxidizing conditions, coupled with high conductivity and low activation energy. In any case, to better understand the potentiality of DST8, it should be tested as anode in a solid oxide fuel cell, that uses standard materials as cathode and electrolyte, to compare obtained performances and aging tests should be performed, to check the effective stability in operative conditions.

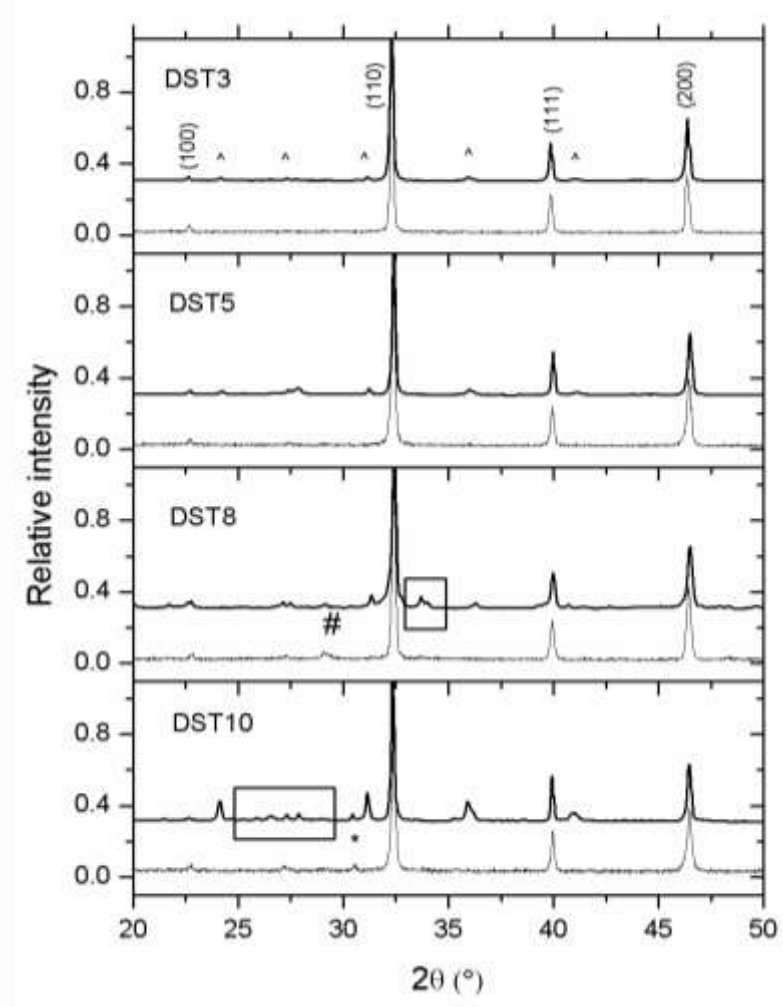

Figure 6.7: Comparison of XRD patterns obtained before (thin line) and after reduction (thick line). Miller indexes of $SrTiO_3$ are also reported with major reflections of TiO_2 (^), Dy_2O_3 (#) and $Dy_2Ti_2O_7$ (*) secondary phases. Peaks of mixed Ti, Sr oxides, different from $SrTiO_3$ are highlighted by rectangles.

6.3 Conclusions

In this chapter, Dy-doped $SrTiO_3$ system was studied for the first time as candidate for anodic materials. Microstrain, crystallite size and density decreased with increasing of Dy content for $x \leq 0.08$, where a minimum was detected for all quantities, and then increased again for $x = 0.10$. Moreover, samples with $x \leq 0.05$, are single phase, while for $x \geq 0.08$ about 6 wt.% of secondary phases are formed. In air, the conductivity is predominantly electronic type for $x \leq 0.05$, becoming ionic for $x \geq 0.08$. It is observed that conductivity, for all compositions, increased passing from air to hydrogen and activation energy decreased. $Dy_{0.05}Sr_{0.95}TiO_{3-\delta}$ shows the highest conductivity in air whereas $Dy_{0.08}Sr_{0.92}TiO_{3-\delta}$ in H_2 atmosphere. Results can be explained by considering different incorporation mechanisms, for different amounts of Dy, particularly simultaneous incorporation at Sr- and Ti-sites, incorporation at Ti-site with oxygen vacancies compensation or incorporation at Sr-site with electron compensation. Some degradation is observed by XRD for $x > 0.08$ after reduction, that increases by increasing Dy content, being still limited in DST8 and not affecting conductivity. Hence, DST8 may be considered as a promising anode material for solid oxide fuel cells. In the future, it will be tested in operative SOFC conditions to check performances. Moreover, aging tests will be performed, to check the effective stability.